Vapor bubble generation around gold nanoparticles and its application to damaging of cells

M. Kitz,[1] S. Preisser,[1] A. Wetterwald,[2] M. Jaeger,[3] G. N. Thalmann,[4] and M. Frenz[1,5,*]

[1]*Institute of Applied Physics, University of Bern, Sidlerstrasse 5, 3012 Bern, Switzerland*
[2]*Department of Clinical Research, University of Bern, Murtenstrasse 35, 3010 Bern, Switzerland*
[3]*Now at the Institute for Cancer Research: Royal Cancer Hospital, 123 Old Brompton Road, London SW7 3RP, UK*
[4]*Department of Urology, University of Bern, Inselspital, 3010 Bern, Switzerland*
[5]*Corresponding author Phone: + 41 31 631 8943, Fax: + 41 31 631 3765*
**martin.frenz@iap.unibe.ch*

Abstract: We investigated vapor bubbles generated upon irradiation of gold nanoparticles with nanosecond laser pulses. Bubble formation was studied both with optical and acoustic means on supported single gold nanoparticles and single nanoparticles in suspension. Formation thresholds determined at different wavelengths indicate a bubble formation efficiency increasing with the irradiation wavelength. Vapor bubble generation in Bac-1 cells containing accumulations of the same particles was also investigated at different wavelengths. Similarly, they showed an increasing cell damage efficiency for longer wavelengths. Vapor bubbles generated by single laser pulses were about half the cell size when inducing acute damage.

OCIS codes: (170.0170) Medical optics and biotechnology; (170.5180) Photodynamic therapy.

References and links

1. A. Agarwal, S. W. Huang, M. O'Donnell, K. C. Day, M. Day, N. Kotov, and S. Ashkenazi, "Targeted gold nanorod contrast agent for prostate cancer detection by photoacoustic imaging," J. Appl. Phys. **102**(6), 064701–064704 (2007).
2. J. A. Copland, M. Eghtedari, V. L. Popov, N. Kotov, N. Mamedova, M. Motamedi, and A. A. Oraevsky, "Bioconjugated gold nanoparticles as a molecular based contrast agent: implications for imaging of deep tumors using optoacoustic tomography," Mol. Imaging Biol. **6**(5), 341–349 (2004).
3. E. B. Dickerson, E. C. Dreaden, X. Huang, I. H. El-Sayed, H. Chu, S. Pushpanketh, J. F. McDonald, and M. A. El-Sayed, "Gold nanorod assisted near-infrared plasmonic photothermal therapy (PPTT) of squamous cell carcinoma in mice," Cancer Lett. **269**(1), 57–66 (2008).
4. D. Lapotko, E. Lukianova, M. Potapnev, O. Aleinikova, and A. Oraevsky, "Method of laser activated nano-thermolysis for elimination of tumor cells," Cancer Lett. **239**(1), 36–45 (2006).
5. D. P. O'Neal, L. R. Hirsch, N. J. Halas, J. D. Payne, and J. L. West, "Photo-thermal tumor ablation in mice using near infrared-absorbing nanoparticles," Cancer Lett. **209**(2), 171–176 (2004).
6. L. Tong, Y. Zhao, T. B. Huff, M. N. Hansen, A. Wei, and J. X. Cheng, "Gold Nanorods Mediate Tumor Cell Death by Compromising Membrane Integrity," Adv. Mater. (Deerfield Beach Fla.) **19**(20), 3136–3141 (2007).
7. V. P. Zharov, E. I. Galanzha, E. V. Shashkov, N. G. Khlebtsov, and V. V. Tuchin, "In vivo photoacoustic flow cytometry for monitoring of circulating single cancer cells and contrast agents," Opt. Lett. **31**(24), 3623–3625 (2006).
8. X. Yang, E. W. Stein, S. Ashkenazi, and L. V. Wang, "Nanoparticles for photoacoustic imaging," Wiley Interdiscip Rev Nanomed Nanobiotechnol **1**(4), 360–368 (2009).
9. X. Huang, I. H. El-Sayed, W. Qian, and M. A. El-Sayed, "Cancer cell imaging and photothermal therapy in the near-infrared region by using gold nanorods," J. Am. Chem. Soc. **128**(6), 2115–2120 (2006).
10. C. M. Pitsillides, E. K. Joe, X. Wei, R. R. Anderson, and C. P. Lin, "Selective cell targeting with light-absorbing microparticles and nanoparticles," Biophys. J. **84**(6), 4023–4032 (2003).
11. V. P. Zharov, R. R. Letfullin, and E. N. Galitovskaya, "Microbubbles-overlapping mode for laser killing of cancer cells with absorbing nanoparticle clusters," J. Phys. D Appl. Phys. **38**(15), 2571–2581 (2005).
12. K. R. Rau, P. A. Quinto-Su, A. N. Hellman, and V. Venugopalan, "Pulsed laser microbeam-induced cell lysis: time-resolved imaging and analysis of hydrodynamic effects," Biophys. J. **91**(1), 317–329 (2006).
13. S. Egerev, S. Ermilov, O. Ovchinnikov, A. Fokin, D. Guzatov, V. Klimov, A. Kanavin, and A. Oraevsky, "Acoustic signals generated by laser-irradiated metal nanoparticles," Appl. Opt. **48**(7), C38–C45 (2009).
14. V. P. Zharov, K. E. Mercer, E. N. Galitovskaya, and M. S. Smeltzer, "Photothermal nanotherapeutics and nanodiagnostics for selective killing of bacteria targeted with gold nanoparticles," Biophys. J. **90**(2), 619–627 (2006).

#136327 - $15.00 USD Received 11 Oct 2010; revised 7 Dec 2010; accepted 9 Jan 2011; published 11 Jan 2011

15. J. Rička, "Dynamic light scattering with single-mode and multimode receivers," Appl. Opt. **32**(15), 2860–2875 (1993).
16. M. Ruosch, D. Marti, P. Stoller, J. Rička, and M. Frenz, "Dependence of the multiphoton luminescence spectrum of single gold nanoparticles on the refractive index of the surrounding medium," Proc. SPIE 7032(2008).
17. L. Rayleigh, "On the Pressure developed in a Liquid during the Collapse of a Spherical Cavity," Philos. Mag. **34**, 94–98 (1917).
18. H. Okumura, and N. Ito, "Nonequilibrium molecular dynamics simulations of a bubble," Phys. Rev. E Stat. Nonlin. Soft Matter Phys. **67**(4), 045301 (2003).
19. D. Lapotko, A. Shnip, and E. Lukianova, "Photothermal responses of individual cells," J. Biomed. Opt. **10**(1), 014006–014012 (2005).
20. I. Akhatov, O. Lindau, A. Topolnikov, R. Mettin, N. Vakhitova, and W. Lauterborn, "Collapse and rebound of a laser-induced cavitation bubble," Phys. Fluids **13**(10), 2805–2819 (2001).
21. M. S. Hutson, and X. Ma, "Plasma and cavitation dynamics during pulsed laser microsurgery in vivo," Phys. Rev. Lett. **99**(15), 158104 (2007).
22. T. Asshauer, G. Delacrétaz, E. D. Jansen, A. J. Welch, and M. Frenz, "Pulsed holmium laser ablation of tissue phantoms: correlation between bubble formation and acoustic transients," Appl. Phys. B **65**(4-5), 647–657 (1997).
23. M. Frenz, H. Pratisto, F. Könz, E. D. Jansen, A. J. Welch, and H. P. Weber, "Comparison of the effects of absorption coefficient and pulse duration of 2.12 mm and 2.79 mm radiation on laser ablation of tissue," IEEE J. Quantum Electron. **32**(12), 2025–2036 (1996).
24. A. Vogel, W. Lauterborn, and R. Timm, "Optical and acoustic investigations of the dynamics of laser-produced cavitation bubbles near a solid boundary," J. Fluid Mech. **206**(-1), 299–338 (1989).
25. C. E. Brennen, *Cavitation and Bubble Dynamics* (Oxford University Press, New York, 1995), Chap. 1.10.
26. S. C. Hendy, "A thermodynamic model for the melting of supported metal nanoparticles," Nanotechnology **18**(17), 175703 (2007).
27. V. P. Zharov, E. N. Galitovskaya, C. Johnson, and T. Kelly, "Synergistic enhancement of selective nanophotothermolysis with gold nanoclusters: potential for cancer therapy," Lasers Surg. Med. **37**(3), 219–226 (2005).
28. B. Khlebtsov, V. P. Zharov, A. Melnikov, V. Tuchin, and N. G. Khlebtsov, "Optical amplification of photothermal therapy with gold nanoparticles and nanoclusters," Nanotechnology **17**(20), 5167–5179 (2006).

1. Introduction

Recently gold nanoparticles have received much attention because of the phenomenon of plasmon resonance, which results in strong absorption at specific wavelengths. Laser irradiation of such particles allows for high and targeted heat deposition making the particles suitable agents for contrast enhancement in optoacoustics or for mechanically damaging biological tissue [1–7]. Common to these applications is that nanosecond laser pulses close to the particles' resonant wavelength are employed to rapidly heat the particles and their surroundings. In optoacoustics the rapid heating causes quick thermal expansion thus generating pressure transients with ultrasound wavelengths.By conjugating the nanoparticles to antibodies or proteins that bind to antigens over-expressed on tumor cells, selective detection can be achieved, rendering molecular optoacoustic imaging possible. The lack of endogenous absorbers in tumors in an early stage at which microvasculature has not yet developed can thus be overcome, making it possible to detect the tumor [1,2,8].

For therapeutic applications the selectively bound nanoparticles are employed as heat sources. By continuous irradiation a temperature rise of tens of degrees can be induced, which causes thermal damage to the cells [5,6,9]. With pulsed irradiation at sufficiently high radiant exposures the particles serve as nuclei for transient vapor bubbles that mechanically damage the targeted cells [4,10,11]. The effect of short-lived vapor bubbles on cells was, for example, shown by Rau et al. [12] who presented experiments that indicate shear stresses during vapor bubble expansion and collapse to be the primary cell damage mechanism under nanosecond pulse irradiation.

Though many experiments with targeted cells under pulsed irradiation have been performed, there are still open questions regarding the process of vapor bubble mediated damage. For example, it is not clear whether all bubbles lead to cell damage or what the conditions for bubble formation are and how it is influenced by the irradiation wavelength.

Little information is available to answer these questions. Egerev et al. [13] calculated a lower limit of 36 mJ/cm^2 for the vapor bubble formation threshold from a theoretical model and measured a threshold of 50 mJ/cm^2 for the giant optoacoustic effect, i.e. a pressure amplitude which exceeded that from thermoelastic expansion and was attributed to vapor

#136327 - $15.00 USD Received 11 Oct 2010; revised 7 Dec 2010; accepted 9 Jan 2011; published 11 Jan 2011

bubble formation. Using different experimental setups, damage thresholds have been reported ranging from 80 mJ/cm^2 to 500 mJ/cm^2 [4,10,11,14].

It is, however, difficult to correlate these results since different wavelength, pulse lengths, pulse numbers during irradiation and particle sizes and conjugation states, i.e. with and without antibodies, were used. Also, regarding vapor bubble formation thresholds differences may be due to variations in detection sensitivity of the individual experimental setups and to differences between the nanoparticles themselves, even though their nominal properties seem to be the same.

By using identical particles and irradiation parameters for investigating the interaction processes with single gold nanoparticles and cells, we address some of these differences to improve the understanding of how vapor bubble formation around single particles and cell damage are related.

In this work we comprehensively studied the interaction of spherical gold nanoparticles of 90 nm diameter with nanosecond laser pulses near the plasmon resonance wavelength. An investigation of laser-induced vapor bubbles and pressure transients is first presented for single particles supported by a cover slip. Then, we compare the bubble formation threshold of a single nanoparticle with that in a particle suspension. Finally we report on measurements of vapor bubble formation in cells that had been incubated with nanoparticles of the same size.

2. Materials and methods

All experiments were performed with spherical gold particles of 90 nm diameter (Nanoparticles Inc.). The nanoparticle size was verified using a fiber based dynamic light scattering setup [15] and ALV5000 digital correlator. Extinction measurements performed on a Perkin-Elmer spectrophotometer (lambda 9) confirmed the extinction spectrum calculated for particles of this size applying Mie theory. The particle concentrations were determined from extinction spectra using the calculated extinction cross-section.

Samples for single particle experiments were spin-coated onto a coverslip and subsequently immersed in purified and deionized water. A confocal scanning microscope (described in [16]) was used to verify that spin-coating yielded single particle distributions.

The nanoparticle suspensions were prepared from the original sample by diluting with purified and deionized water to a concentration of 10^8 particles/ml.

2.1. Single nanoparticle experiments

For observation of vapor bubble formation around single nanoparticles we set up an inverted microscope as shown in Fig. 1a. A 1.2 NA water immersion microscope objective and a darkfield epi-illumination scheme allowed for observation of single nanoparticles. The excitation laser, an optical parametric oscillator (OPO) pumped by a frequency tripled Nd:YAG (5 ns pulse duration), was used for irradiation at 498 nm, 532 nm, 600 nm and two different wavelengths in the near infrared, 755 and 780 nm. The beam was focused to a spot of 2.5 μm diameter (FWHM) on the sample through the microscope objective. The pulse energy was adjusted using a combination of a half-wave plate and a Glan-Taylor prism (GTP). The radiant exposure at the particle site was varied in a large interval of 30 mJ/cm^2 to 7.60 J/cm^2 when irradiating at 532 nm. At the other wavelengths intervals of 70 to 190 mJ/cm^2 (498 nm), 50 to 220 mJ/cm^2 (600 nm) and 250 to 1000 mJ/cm^2 (NIR) were used. A short-pulse dye laser (Rhodamine 6G, 700 ps) synchronized with the excitation laser at a tunable delay was employed for flash photography of vapor bubbles.

#136327 - $15.00 USD Received 11 Oct 2010; revised 7 Dec 2010; accepted 9 Jan 2011; published 11 Jan 2011

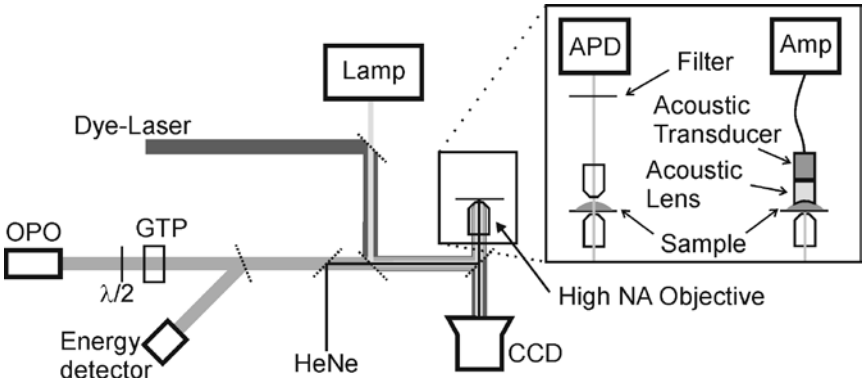

Fig. 1. Microscopic setup, cw HeNe laser for targeting and bubble detection; OPO: 5 ns pulsed excitation beam; Lamp: standard cw illumination; dye-laser for optional 700 ps illumination; λ/2 + Glan-Taylor prism (GTP) for energy adjustment; with alternative detectors: APD for transmitted laser detection or acoustic transducer with amplifier for pressure transient detection.

Additionally, a continuous wave (cw) HeNe laser focused to a spot of 1 μm diameter was confocally aligned with the excitation beam. The reflection of the HeNe laser beam at the coverslip surface marked the focus of the excitation laser and thus was used for aiming. Within the focus area of the laser a nanoparticle appeared as a bright spot due to back-scattering of the HeNe laser beam which allowed for precise alignment of the particle with respect to the center of the focal spot of the OPO beam.

The main purpose of the HeNe laser, though, was to measure the lifetime of the laser-induced vapor bubble. Vapor bubble formation around the nanoparticle caused a change of the index of refraction around the nanoparticle and therefore a decrease of the intensity of the transmitted light which was collected with a 10x microscope objective and imaged onto an avalanche photo diode (APD). A narrow band interference filter at 633 nm placed in front of the APD blocked the light from the OPO. Thus the time during which a vapor bubble was present in the focus area was reproduced by the time of the transient drop in transmission of the HeNe laser beam.

The lifetime of the vapor bubble was recorded as a function of the radiant exposure for a few hundred particles. Each nanoparticle was irradiated only once regardless of the experimental outcome to avoid distortion of the results by irradiating a particle possibly structurally altered by the previous laser pulse. The results were analyzed regarding the probability of bubble occurrence as a function of the applied radiant exposure. Due to the statistical nature of the bubble formation process this function resembles a step function convoluted with a statistical distribution function. We modeled the function assuming a logistic distribution. From the fit to the data the bubble formation threshold was taken as the 50% probability point.

Flash photography and bubble lifetime measurement were performed simultaneously. Adjusting the delay of the ps-laser pulse allowed for timing of the photography within the bubble lifetime interval Δt.

Alternatively to the lifetime measurement based on the HeNe laser transmission, an acoustic pressure transducer (Panametrics V311-SU, central frequency 10 MHz/100% bandwidth) was used to record the pressure transients generated upon irradiation of the nanoparticle. The transducer was focused onto the focal spot of the excitation laser (illustrated in Fig. 1b) with a custom-made, acrylic acoustic lens (f = 10 mm). The pressure transients were measured as a function of the laser radiant exposure.

2.2. Nanoparticle suspension experiments

For the previously described single particle experiments the nanoparticles had been spin-coated onto a coverslip, which means that bubble formation was confined by the glass

#136327 - $15.00 USD Received 11 Oct 2010; revised 7 Dec 2010; accepted 9 Jan 2011; published 11 Jan 2011

interface. To overcome this geometrical restriction we also performed measurements of the bubble formation threshold and pressure transient generation with nanoparticles in suspension.

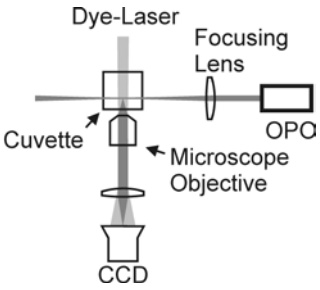

Fig. 2. Irradiation of nanoparticle suspension, 10x10 mm^2 cuvette, 80x long working distance, 0.9 NA objective; optional 700 ps illumination; acoustic transducer below the cuvette bottom (not shown).

The setup is shown in Fig. 2. The same OPO as in the single particle experiments was used for excitation with single laser pulses. The OPO laser beam was focused to a spot diameter of 100 µm with a Rayleigh range of 3 mm inside a standard cuvette (polystyrene, 10x10x50 mm^3) containing the nanoparticle suspension. Perpendicular to the excitation beam, an area of approximately 130 µm length along the optical axis of the beam waist was imaged onto a CCD camera. Since the Rayleigh range of the excitation beam was much longer than the 130 µm, the radiant exposure profile of the excitation laser was assumed to be constant within the imaged area. The radiant exposure was then determined from a calibrated energy measurement and the separately measured beam profile at the waist.

To detect the occurrence of laser-induced bubbles the short-pulse dye-laser was employed for transverse (brightfield) illumination of the imaged area at a delay of 20 ns after the excitation pulse. In these images vapor bubbles appeared as spots of reduced transmission due to their highly increased scattering compared to bare nanoparticles. The delay of 20 ns was chosen as a compromise: If the delay was chosen too long, all the small bubbles having a short lifetime could not be detected. If, on the other hand, the delay was too short, the bubbles had not yet expanded to a detectable size at the time of imaging. To account for the statistical nature of bubble formation, series of images at constant radiant exposure were taken. These images were analyzed to determine the radiant exposure of the bubble formation threshold.

For the measurement of the pressure transient generation in nanoparticle suspensions the bottom of the cuvette was replaced by a thin film with low acoustic impedance (Mylar, 23 µm, DuPont). The ultrasound transducer was placed below the cuvette with water as coupling medium.

2.3. Cell irradiation experiments

The effect of nanoparticle irradiation on cells was investigated with Bac-1 cells (macrophages). The cells were cultured in alpha MEM (Biochrom, Berlin, Germany) supplemented with 15% FBS (Biochrom) and 8000 U/ml macrophage colony-stimulating factor-1 (CSF-1, kindly provided by Cetus Corporation, CA). Cells were plated in 3 cm diameter Petri dishes and grown for 1-2 days before incubation with nanoparticles. The cells were incubated with 2 ml PBS/1% BSA and different amounts of nanoparticle suspension from 20 to 150 µl ($6.4 \cdot 10^{10}$ particles/ml) for 3½ hours. After incubation, excess nanoparticles were removed by thoroughly rinsing with PBS. Control samples were prepared by the same procedure without gold nanoparticles in the medium during the incubation period.

Single cells were irradiated with a single shot from the OPO that was focused to a spot (top-hat profile) of 35 µm diameter. Simultaneously, pressure transients were measured with an acoustic transducer (central frequency 2.25 MHz) focused via an acoustic lens and aligned confocally with the irradiation spot. After irradiation the cells were treated with trypan blue to stain cells that suffered membrane damage. Images of the cells were taken before irradiation and after the staining procedure.

#136327 - $15.00 USD Received 11 Oct 2010; revised 7 Dec 2010; accepted 9 Jan 2011; published 11 Jan 2011

3. Results

3.1. Single nanoparticle measurements at 532 nm

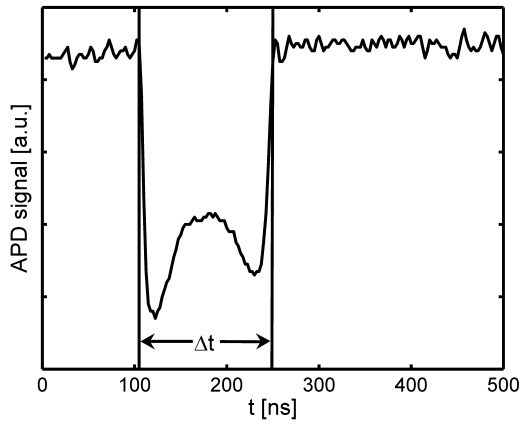

Fig. 3. APD signal of probe laser intensity when irradiating a targeted nanoparticle with radiant exposures above the bubble formation threshold.

Figure 3 shows an example of the HeNe laser signal from which the bubble lifetime Δt was taken for a bubble generated around a single nanoparticle. The signal has a local extremum at around ½Δt related to the maximum bubble expansion. This extremum occurs when the bubble diameter exceeds the probe laser spot so that the diffractive effect of the bubble boundary on the probe beam decreases with increasing bubble radius and therefore decreasing curvature. The maximum bubble size was determined from images taken at this time (see Fig. 4, inset). For comparison, the maximum bubble size r_c was calculated from the measured lifetime as suggested by Rayleigh's equation [17]

$$r_c = \tfrac{1}{0.915} \cdot \tfrac{1}{2} \Delta t \cdot \sqrt{p_0 / \rho}, \qquad (1)$$

ρ being the density of the medium (10^3 kg/m^3) and p_0 the pressure at infinity (10^5 N/m^2). Both radii taken from several measurements are shown in Fig. 4. The comparison reveals that the measured radii are smaller than the values expected from Rayleigh's equation (Eq. (1)).

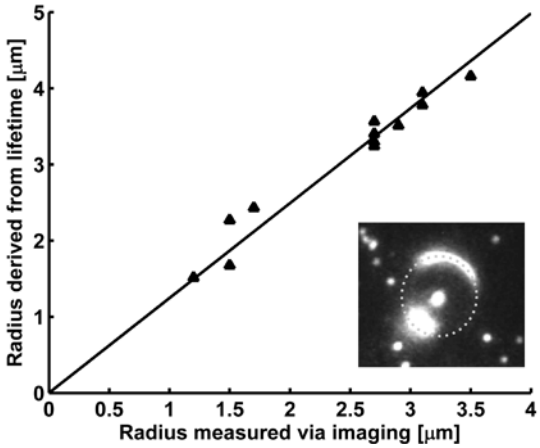

Fig. 4. Triangles: Comparison of bubble radius determined from measurement r_m and calculated from the measured lifetime r_t using Rayleigh's equation (see text); solid line: linear fit to experimental data, $r_m/r_t = 1.25 \pm 0.02$; inset: dark-field image of a vapor bubble (radius; dotted circle indicates the complete bubble boundary.

#136327 - $15.00 USD Received 11 Oct 2010; revised 7 Dec 2010; accepted 9 Jan 2011; published 11 Jan 2011

As shown in Fig. 5 the bubble lifetime increases with increasing radiant exposure. Figure 6 shows the probability of bubble occurrence as a function of the radiant exposure and a logistic fit to the experimental data. The threshold for vapor bubble formation at a single nanoparticle (50% probability) was found to be 60 ± 4 mJ/cm^2.

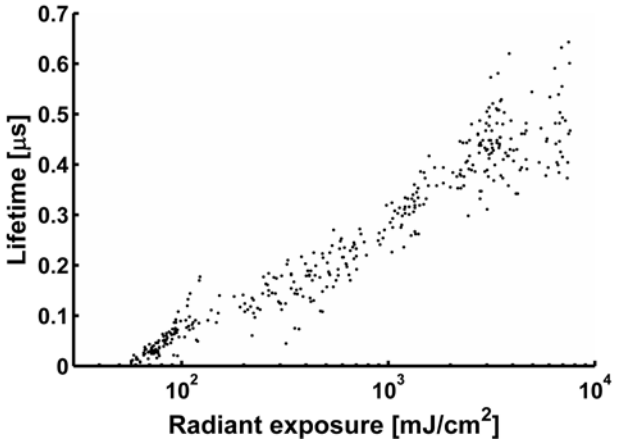

Fig. 5. Bubble lifetime versus radiant exposure in a semi-log plot for irradiation at 532 nm, sample size N = 400.

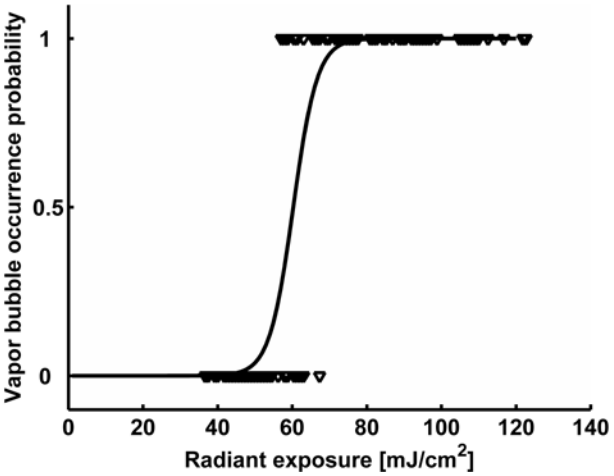

Fig. 6. Observed bubble formation versus radiant exposure at 532 nm (triangles) and fit of a logistic distribution (solid line), 50% occurrence probability at 60 ± 4 mJ/cm^2.

#136327 - $15.00 USD Received 11 Oct 2010; revised 7 Dec 2010; accepted 9 Jan 2011; published 11 Jan 2011

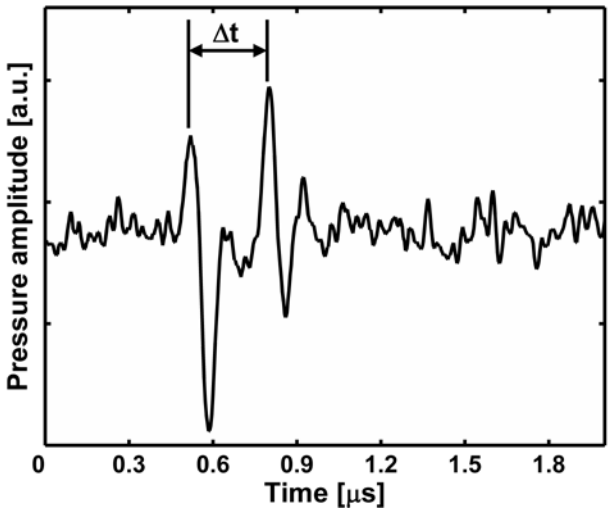

Fig. 7. Pressure transient from bubble formation and collapse at a single nanoparticle; the bubble lifetime Δt is taken from the delay between the transients.

The pressure measurements on single particles showed two distinct transients of the same polarity (see Fig. 7). The time delay between the two pressure transients increased with radiant exposure and closely corresponds with the lifetime of the vapor bubble measured with the cw probing setup (compare Fig. 5). The relation of the time between the two pressure transients and the peak-to-peak amplitude of the first pressure transient is shown in Fig. 8. Due to the transducer properties (10 MHz centre frequency) only lifetimes longer than 100 ns could be measured. These lifetimes occurred for radiant exposures above ~110 mJ/cm^2.

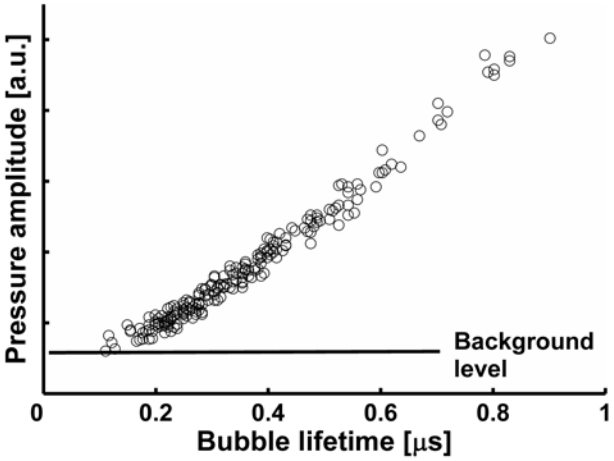

Fig. 8. Peak-to-peak amplitude of the pressure pulse from bubble formation around single particles versus bubble lifetime.

3.2. Nanoparticle suspension measurements at 532 nm

Measurements with particle suspensions yielded very similar results as the single particle experiments. From vapor bubble detection by flash photography an upper limit for the bubble formation threshold was determined to be 80 ± 5 mJ/cm^2. Additional data on the threshold was gained from pressure measurements. The pressure signal from irradiated particles in suspension showed a strong initial transient followed by unspecific pressure variations. This initial pressure transient is a superposition of the transients generated by the formation of

#136327 - $15.00 USD Received 11 Oct 2010; revised 7 Dec 2010; accepted 9 Jan 2011; published 11 Jan 2011

bubbles around many particles immediately following the laser pulse. As many particles are irradiated with different radiant exposures across the Gaussian laser beam, differently sized bubbles are generated which results in bubble collapse signals occurring at different delays and thus average out. The dependence of the peak-to-peak amplitude of the initial transient in the recorded signal on the maximum radiant exposure is shown in Fig. 9 (circles). The plot reveals that pressure transients can be detected if the radiant exposure exceeds 60 ± 5 mJ/cm^2.

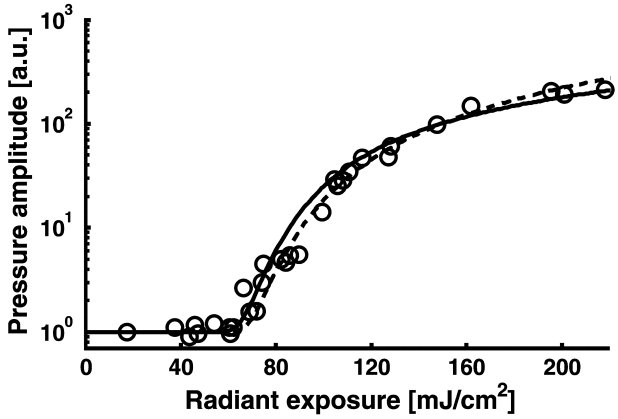

Fig. 9. Pressure amplitude from nanoparticle suspension; circles: data from measurements, solid line: extrapolated from measurements with single particles, dashed line: extrapolated using p~H-H_{th}, see text for details; the onset of bubble formation manifests itself as a sudden increase of the detected pressure amplitude.

3.3. Single nanoparticle measurements at different wavelengths

Since irradiation in the NIR is more interesting for medical applications due to the lower absorption of these wavelengths by biological tissue, we also examined the vapor bubble formation thresholds at other wavelengths than 532 nm. The results are shown in Table 1 as well as the absorption cross-sections calculated according to Mie theory.

Table 1. Threshold radiant exposures for vapor bubble formation around single 90 nm gold nanoparticles at different irradiation wavelengths

Irradiation wavelength [nm]	498	532	600	755	780
Threshold [mJ/cm^2]	110 ± 6	60 ± 5	70 ± 6	350 ± 50	440 ± 80
Absorption cross-section [cm^2]	$1.6\cdot10^{-10}$	$2.0\cdot10^{-10}$	$8.6\cdot10^{-11}$	$5.6\cdot10^{-12}$	$4.7\cdot10^{-12}$

Obviously, the threshold radiant exposure for vapor bubble formation is lowest close to the surface plasmon resonance of the particles and higher at wavelength with lower absorption cross-section. But while the absorption cross-section at 780 nm is more than 40 times smaller than at 532 nm, the vapor bubble formation threshold of 440 mJ/cm^2 is only 7 times higher at that wavelength. Even at 600 nm where the absorption cross-section is 2.3 times smaller, the threshold of 70 mJ/cm^2 is only a little higher than at 532 nm. On the other hand, at 498 nm the threshold is almost twice the value at 532 nm although the absorption cross-section is only 20% smaller.

3.4. Cell irradiation experiments

To get a first insight into biological effects of vapor bubble formation, we also conducted a series of preliminary experiments with cells, namely with macrophages (Bac-1) that had been incubated with a suspension of the 90 nm nanoparticles. These cells are capable of easily internalizing the nanoparticles via phagocytosis without the need for targeting methods as has been verified by multiphoton luminescence and TEM imaging. Particles have been found to

#136327 - $15.00 USD Received 11 Oct 2010; revised 7 Dec 2010; accepted 9 Jan 2011; published 11 Jan 2011

be mostly accumulated within lysosomes of 500 to 1500 nm diameter. Based on the TEM images we roughly estimated that three quarters of the lysosomes contain 50-200 particles while the remaining quarter of them contains up to 1500 particles. Each cell usually shows 2-5 lysosomes of various sizes in a single TEM imaged section.

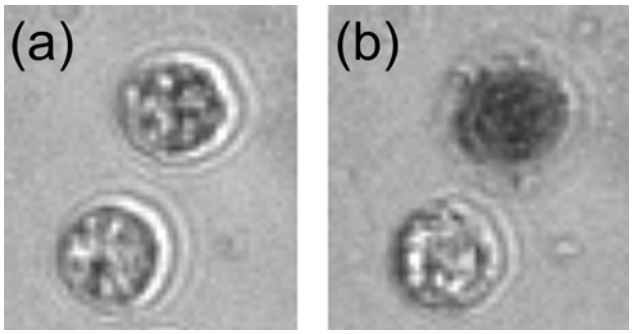

Fig. 10. (a) cells before irradiation, (b) the same cells after irradiating only the upper cell with about 100 mJ/cm^2 and staining with trypanblue; cells had been incubated with $0.6 \cdot 10^9$ particles/ml for 3.5 hours.

Figure 10(a) and 10(b) shows pictures of cells incubated with gold nanospheres ($0.6 \cdot 10^9$ particles/ml concentration) before and after irradiation of one of cells with a single laser pulse of a radiant exposure of 100 ± 10 mJ/cm^2. The staining of the cell after treatment with trypan blue (Fig. 10b) indicates damage to the membrane. From a series of measurements at different radiant exposures and with different cells the threshold (50% probability) for the staining was determined. In samples incubated with different particle concentrations (0.6 to $4.5 \cdot 10^9$ particles/ml) for 3.5 hours cell damage thresholds of 40-140 mJ/cm^2 were found. The threshold for detectable pressure signals indicating the generation of a vapor bubble (50% probability) was about 25% to 50% lower than the threshold for staining that visualized the acute cell damage. The pressure measurements showed two transients of similar shape whose time delay increased with increasing radiant exposure. At the threshold for staining, the delay between the two transients was 0.6 to 0.8 μs in all samples, independent of the particle concentration used.

Cells in the control sample without nanoparticles could not be damaged and did not produce any pressure transients even with the highest radiant exposure of 600 mJ/cm^2.

Damage thresholds at 600 and 755 nm irradiation were found to be 45 and 130 mJ/cm^2, respectively, for cells incubated for 3.5 hours at $4 \cdot 10^9$ particles/ml. That means that the damage threshold at 600 nm was practically the same as for 532 nm, whereas it was about 3 times higher for near infrared irradiation.

4. Discussion

The results obtained from the single particle experiments provide a coherent picture of bubble formation. We observed a fast transient decrease in the intensity of the transmitted HeNe laser after irradiating a single nanoparticle with a laser pulse of a radiant exposure exceeding 60 mJ/cm^2. The duration of this intensity decrease marks the lifetime of the laser induced vapor bubble. It shows a symmetric dependence on time, consistent with the temporal evolution of the transient vapor bubble size [18]. A change in the index of refraction due to heating of the water, on the other hand, would have caused an asymmetric signal shape with a steep initial slope and an exponential relaxation due to the heat dissipation by diffusion [19]. Additional second and third transient intensity drops that occasionally appeared at high radiant exposures with much smaller amplitude visualized the occurrence of bubble rebounds [20].

By using the pressure transducer, we detected two distinct pressure transients upon irradiation, whose time delay perfectly coincided with the length of the HeNe laser transmission drop. Interestingly, the transients are of the same polarity and their shape does not change with their mutual delay, which means that they are not related to volume changes

#136327 - $15.00 USD Received 11 Oct 2010; revised 7 Dec 2010; accepted 9 Jan 2011; published 11 Jan 2011

of the bubble. Instead, the pressure transients are associated with the initial and final stages of the expansion and collaps, which are known to create strong acoustic transients [13,21–23]. We further noticed that the peak-to-peak amplitudes of both transients increased proportionally to the bubble lifetime (see Fig. 8) while their ratio approaches unity with increasing bubble lifetime (not shown). The sequence of two pressure transients of similar amplitude, which represent a distinct signature of a transient vapor bubble, therefore allows us to identify the occurrence of single vapor bubbles in the cell experiments.

Flash photography of the bubbles further enabled us to relate the lifetime of a vapor bubble to its size. The bubble radius obtained from an image and the bubble radius calculated from the measured lifetime using Eq. (1) nicely match (see Fig. 4). The fact that the measured radius was about 20% smaller than expected based on the lifetime measurements and Rayleigh's equation is probably a consequence of the bubbles being in contact with the glass interface. Rayleigh's equation was derived for free spherical bubbles and may not be strictly applicable to our case. It has been observed before that the expansion and collapse of a bubble close to a surface are damped compared to one in free liquid [24]. This can explain the lower measured radius compared to the calculation from the lifetime. Another reason for the slight discrepancy between the measured and the calculated bubble lifetime might be caused by the uncertainty to precisely determine the maximum bubble expansion from the flash photography images. Taking this into account our results from cw laser probing and flash photography of the bubbles show very good agreement.

These experiments demonstrate that we can detect vapor bubbles around single nanoparticles using two different methods and estimate their size from measured lifetimes. The HeNe laser probing provides a sensitive tool capable of measuring vapor bubble lifetimes as short as 10 ns which correspond to a vapor bubble diameter of around 110 nm calculated with Eq. (1). Whereas the optical method requires a probe laser in a transmission setup, the acoustic measurement is basically applicable from any direction. This made the pressure measurement more flexible and easier to implement in our microscopic setup for cell experiments.

Since a boundary layer close to a nanoparticle may influence vapor bubble nucleation [25] or facilitate local melting of the particle [26], experiments to measure the vapor bubble formation threshold and pressure transients were also performed with particle suspensions.

In the nanoparticle suspension vapor bubbles were detected at radiant exposures above 80 mJ/cm^2 by brightfield flash photography. This method is less sensitive than the focused laser probing on the single particles and therefore yields just an upper limit for the threshold.

The pressure measurements showed transients consistent with bubble formation at 60 mJ/cm^2. This was found by estimation of the pressure amplitude in the irradiated suspension based on results from the measurements with single particles:

The amplitude $\hat{A}$ of the transducer signal is proportional to the pressure transient which is the sum of the transients $\hat{p}_i$ from all N irradiated particles in the cuvette. $\hat{p}_i$ can be deduced from the proportionality of pressure amplitude and lifetime known from Fig. 8 and from a function $t(H)$ approximated to the data shown in Fig. 5 which describes the dependency of the lifetime on the radiant exposure. This is summarized in Eq. (2):

$$\hat{A} \propto \sum_{i=1}^{N} \hat{p}_i \propto \sum_{i=1}^{N} t(H_i) \rightarrow \hat{A} \propto \int t(H(n))dn, \tag{2}$$

where $H(n)$ denotes the radiant exposure at the site of the n-th particle. The integration over particles can be replaced by an integration over the volume.

$$\hat{A} \propto \int t(H(\vec{r}))\frac{dn}{dV}dV \tag{3}$$

#136327 - $15.00 USD Received 11 Oct 2010; revised 7 Dec 2010; accepted 9 Jan 2011; published 11 Jan 2011

The radiant exposure $H(\vec{r})$ in Eq. (3) is given by the pulse energy *E* and the beam profile $I(\vec{r})$, whereas the particle concentration *dn/dV* can be regarded as constant, yielding

$$\hat{A} \propto \int t(I(\vec{r}) \cdot E) dV. \tag{4}$$

The beam profile $I(\vec{r})$ was measured with a CCD camera. The pulse energy *E* was used as a parameter. Equation (4) can be rewritten as

$$\hat{A}(H) = const \cdot \int t(I(\vec{r}) \cdot E) dV. \tag{5}$$

Equation (5) was then fitted to the experimental data by varying the constant. For the visualization and comparison with experimental data, the pulse energy is substituted by the peak radiant exposure $H = E \cdot \max(I(\vec{r}))$.

The result is shown in Fig. 9 as a solid line. It shows good agreement with the measurement and thus indicates that our calculation is based on a sensible assumption for pressure transient generation, which means that the transients in fact stem from formation and collapse of vapor bubbles.

The same result is obtained when $\hat{A}(H)$ is calculated based on a theoretical approach reported by Egerev et al. [13]. As a simplification of their theoretical deduction of the pressure amplitude caused by vapor bubble formation, they found a linear dependency of the pressure amplitude on the radiant exposure, *H*, exceeding the bubble formation threshold H_{th}, i.e. $p \propto (H - H_{th})$. The dotted line in Fig. 9 shows the result of this calculation in which $H - H_{th}$ is used instead of $t(H)$ with a bubble formation threshold H_{th} of 60 mJ/cm^2. It also matches the experimental results very well thus justifying the assumed radiant exposure threshold H_{th} for bubble formation.

Hence we have shown that measurements on single particles and on particles in suspension yielded the same value of 60 ± 5 mJ/cm^2 for the vapor bubble formation threshold. Therefore we conclude that the solid boundary in the single particle experiment, though it may have influenced the bubble lifetime, had no significant influence on the bubble formation threshold.

After investigating vapor bubble formation close to the surface plasmon resonance wavelength we extended our research to near infrared wavelengths that are more interesting for certain biological applications. Data on off-resonant excitation is hard to find in literature, probably since it is considered inefficient because of the low absorption cross-section. This expectation is based on the idea that vapor bubble formation is a thermal process, which means that the heat absorbed in the particle is transferred to the water raising its temperature up to the point of evaporation. If vapor bubble formation worked like that, using the same laser at different wavelengths the same energy deposition $Q = \sigma_{abs} H$ should have the same effect.

Our data (Table 1) indeed shows an increase of the thresholds upon departure from the resonance, but surprisingly, the threshold radiant exposure did not change by the same factor as the absorption cross-section when changing the irradiation wavelength. This indicates that vapor bubble formation is not only a thermal process. We suspect that also the local field strength affects bubble formation and are currently working on the theoretical explanation.

Our primary interest is the application of vapor bubble formation for medical therapy. Based on the presented results we assume that the threshold for bubble formation around a single nanoparticle is not heavily influenced by the properties of biological tissue and therefore is expected to be around 60 mJ/cm^2 as well when irradiating at 532 nm. Considering the fact that vapor bubbles generated at a radiant exposure close to the formation threshold are probably far too small to damage the targeted cells, we expect even higher values for the damage threshold of cells.

#136327 - $15.00 USD Received 11 Oct 2010; revised 7 Dec 2010; accepted 9 Jan 2011; published 11 Jan 2011

Our experiments with macrophages that had been incubated with the same nanoparticles, though, yielded even lower thresholds for acute cell damage than the single particle vapor bubble formation thresholds. It seems reasonable to assume that this difference is caused by accumulation of particles in lysosomes in the cells. In TEM images of Bac-1 cells we found large lysosomes of up to micrometer size depending on the amount of nanoparticles available during incubation. It has been pointed out that aggregation of particles inside cells lowers the damage threshold [27] which apparently happened here.

Further information on the damage process was gained from pressure measurements during irradiation. The recorded pressure signals showed two separate transients of identical shape and often of similar amplitude, especially for high radiant exposures. As seen in the single particle experiments such transients are signs of bubble formation and collapse. A detailed examination of the delay between the two transients revealed that cell damage always occurred for bubble diameters exceeding about half the diameter of the cell.

The lowest threshold for cell damage upon 532 nm irradiation we found was about 40 mJ/cm^2 for cells incubated with the highest nanoparticle concentration. This value is smaller than results previously reported in the literature for similar experiments. Lapotko et al. [4] reported cell damage above 1 J/cm^2 and bubbles in tumor cells at radiant exposures of 100-300 mJ/cm^2 using 30 nm spherical gold particles. Zharov et al. [14] suggested induction of bubble formation around 30-40 nm gold spheres at high particle density and a radiant exposure of 500 mJ/cm^2 to damage cells.

We guess that the strong accumulation of nanoparticles in the macrophages are the key factor that allows for the lower damage threshold. High particle numbers within a small volume can cause a large temperature rise even at relatively low radiant exposures. Evidence for this and a more detailed discussion of the accumulation effects will be provided in a forthcoming publication.

However, lowering the vapor bubble formation threshold might not be the only effect of the particle accumulation. Since it has been reported before that plasmon resonances of particle aggregates were shifted towards the near infrared compared to the single particles [28], it could be advantageous to irradiate the Bac-1 cells at longer wavelengths. Therefore we also performed the cell irradiation experiments at 600 nm and 755 nm with cells incubated at the highest nanoparticle concentration of $\cdot 10^9$ particles/ml. At 600 nm the damage threshold (45 mJ/cm^2) was practically the same as for 532 nm. At 755 nm the threshold was found to be about 130 mJ/cm^2. Vapor bubbles at the damage thresholds were found to be of the same size as observed at 532 nm. The similarity of the thresholds measured for 532 nm and 600 nm may be a result of a shift in the absorption peak but cannot be regarded as significant considering that the threshold values for vapor bubble formation around single particles were also quite similar. However, the damage threshold in the NIR is surprisingly low. Whereas at 532 and 600 nm the damage threshold is 75% of the single particle bubble formation threshold it is 35% at 755 nm. That means that like observed when irradiating single particles vapor bubble formation is also more efficient in the near infrared when irradiating accumulated particles. Heat deposition or bubble nucleation or maybe both are apparently enhanced at longer wavelengths.

These effects should be taken into account when designing a medical application with any type of nanoparticles. However, more research is necessary to clarify these issues for other nanoparticle-laser systems.

5. Conclusion

For the development and improvement of biomedical applications such as photo-acoustic imaging or phototherapies the understanding of the interaction of nanoparticles with light is very important. One aspect thereof is the phenomenon of vapor bubble formation upon ns-pulsed irradiation.

We determined the threshold radiant exposure for vapor bubble formation around single 90 nm gold particles in aqueous environment under irradiation with nanosecond laser pulses at different wavelengths. A value of 60 mJ/cm^2 was found for 532 nm, which is close to the

#136327 - $15.00 USD Received 11 Oct 2010; revised 7 Dec 2010; accepted 9 Jan 2011; published 11 Jan 2011

wavelength of the surface plasmon resonance. Values for longer wavelengths were found to be higher than the 60 mJ/cm^2 but lower than expected from a comparison of theoretical absorption cross-sections.

We suspect that the local electric field strength, which is subject to wavelength-dependent enhancement at the nanoparticle's surface plays an important role in the process of vapor bubble formation.

Furthermore, the study of the photoacoustic response from single irradiated particles provided a tool for the identification and the size estimation of transient vapor bubbles. We applied this tool in the irradiation of cells to estimate the size of vapor bubbles leading to cell damage.

We reported experiments with Bac-1 cells that had been incubated at different concentrations with the same nanoparticles as used for the single particle study. They showed that acute damage to the cells from single pulse irradiation depends on the formation of large vapor bubbles with a size on the order of half the cell size. Particle accumulation greatly lowered the threshold for vapor bubble formation, so that cell damage occurred at radiant exposures below the single particle vapor bubble formation threshold.

Comparison of cell damage thresholds at different irradiation wavelengths seem to confirm that vapor bubble formation is enhanced at longer wavelengths.

Acknowledgments

This research was supported in part by the Swiss National Science Foundation (No 205320-116343) and the 6th Framework Programme of the European Commission within the Specific Targeted Research Project No. LSHC-CT-2006-018858 PROMET. We thank D. Marti for his help with multiphoton luminescence imaging.

#136327 - $15.00 USD Received 11 Oct 2010; revised 7 Dec 2010; accepted 9 Jan 2011; published 11 Jan 2011